metals

MDPI

Article

Microstructural and Magnetic Characteristics of High-Entropy FeCoNiMnTi Alloy Produced via Mechanical Alloying

Chérif Ben Ammar [1,2], Nawel Khitouni [1,2], Marzook Alshammari [3], Abdulrahman Alsawi [4], Mohamed Khitouni [5], Joan-Josep Suñol [1,*] and Mahmoud Chemingui [2]

1 Department of Physics, Campus Montilivi, University of Girona, 17071 Girona, Spain; cherif23495@gmail.com (C.B.A.); khitouninawel@yahoo.fr (N.K.)
2 Laboratory of Inorganic Chemistry, LR17-ES-07, Faculty of Science, University of Sfax, Sfax 3018, Tunisia; chmingui_mahmoud@yahoo.fr
3 Microelectronics and Semiconductors Institute, KACST, Riyadh 12354, Saudi Arabia; alshammari@kacst.gov.sa
4 Department of Physics, College of Science, Qassim University, Buraydah 51452, Saudi Arabia; ansaoy@qu.edu.sa
5 Department of Chemistry, College of Science, Qassim University, Buraidah 51452, Saudi Arabia; kh.mohamed@qu.edu.sa
* Correspondence: joanjosep.sunyol@udg.edu

Abstract: In the current study, X-ray diffraction, scanning electron microscopy, and vibrating sample magnetometer techniques were used to examine the impact of milling time on the microstructural and magnetic characteristics of $Fe_{30}Co_{20}Ni_{20}Mn_{20}Ti_{10}$ (at%) produced via mechanical alloying. Results demonstrate that phase change is dependent on up to 30 h of milling. In terms of the hcp-Fe_2Ti intermetallic and the BCC-FeCoNiMnTi supersaturated solid solution, the system maintains its two-phase structure at higher times. Additionally, the final average crystallite size was estimated to be approximately 10 nm, and the lattice strain was found to be between 0.95 and 1.15%. As a function of milling time, the magnetic properties are discussed with the microstructural and crystallographic alterations. The collected powder after 100 h of milling has an Ms value of 28 emu/g and a Hc value of 25 Am^{-1}, which is consistent with exceptional soft magnetics. This is essentially due to the Fe_2Ti intermetallic and the BCC-Fe-based solid solution production, together with the refinement of the crystallite size. Furthermore, the presence of paramagnetic Ti atoms in solid solution and the development of high densities of defects and interfaces have been connected to the low value of Ms.

Keywords: nanostructure; high-entropy alloys; X-ray diffraction; microstructure; scanning electron microscopy; vibrating sample magnetometry

Citation: Ben Ammar, C.; Khitouni, N.; Alshammari, M.; Alsawi, A.; Khitouni, M.; Suñol, J.-J.; Chemingui, M. Microstructural and Magnetic Characteristics of High-Entropy FeCoNiMnTi Alloy Produced via Mechanical Alloying. *Metals* **2024**, *14*, 1302. https://doi.org/10.3390/met14111302

Academic Editors: Cristian Ciobanu and Jiro Kitagawa

Received: 5 September 2024
Revised: 17 October 2024
Accepted: 15 November 2024
Published: 18 November 2024

1. Introduction

The term "high-entropy alloys" (HEAs) refers to alloys that have five or more predominant component elements. These alloys have attracted a lot of attention in recent decades because of their exceptional mechanical qualities, which include excellent wear and corrosion resistance, suitable oxidation resistance, high ductility, high toughness, and high hardness [1–4]. These alloys were developed due to the complexity of their chemical compositions [5]. More alloying elements, however, are possible because the alloy's properties are notably improved when the alloy's mixing enthalpy and entropy both increase [6]. Further, an equiatomic multicomponent alloy made of a disordered solid solution (SS) is the foundation of HEAs. Compared to conventional alloys, random solid solutions are more common than intermetallic compounds because of the high configurational entropy of mixing, which rises with the number of constituent elements. As a result, HEAs allow researchers greater latitude for developing novel alloys with unique features. On the other hand, over a decade ago, Yeh et al. [7] and Cantor et al. [8] announced the formation of

a novel class of multicomponent alloys known as high-entropy alloys (HEAs). A face-centered cubic (FCC) or body-centered cubic (BCC) solid solution, or a duplex (FCC + BCC) solution, is frequently formed by HEAs [9]. Certain additional HEAs have amorphous structures [10].

The effects of the condition's parameters on the microstructure, magnetic, and mechanical properties of multicomponent HEAs alloys have been examined using a range of preparation methods, including the melting and casting route [11–13], the powder metallurgy (PM) route (involving mechanical alloying (MA) [14–16], and consolidation by spark plasma sintering (SPS)) and additive manufacturing (AM) processing techniques [17]. Table 1 summarizes various fabrication methods of a few HEAs [18–30] and their resulting microstructures and the respective phase(s) obtained, as well as the corresponding mechanical properties. The SPS and MA procedures are rapid, economical with materials, and energy-efficient. However, the PM synthesis of HEAs is hampered by contamination from the milling media. On the other hand, the AM manufacturing method has drawn greater interest lately as a way to get around the drawbacks of other synthesis techniques. A flexible manufacturing method, additive manufacturing (AM) can create items with complicated geometry, finer microstructures, mass customization, and economical material use. HEA nanocrystals prepared by MA have gained a lot of attention in addition to bulk HEAs, which make up the majority of HEAs synthesized so far. The incorporation of a nanocrystalline structure greatly enhances the large compositional space and convoluted dimensions of HEAs. Furthermore, nanostructured HEAs have been shown to have superior mechanical properties [31], improved thermal stability [32], and outstanding magnetic behavior [33]. An established technique for producing distinctive nanoscale solid solution structures and a replacement for arc melting and casting in the synthesis of high entropy alloys is mechanical alloying [34,35]. Furthermore, MA has the benefit of prolonged solid solubility, even in immiscible systems. This can be explained by the greater diffusion rates caused by the powder components' nanosize before the alloying process. Consequently, MA increases configurational entropy while simultaneously providing increased stability to solid solution phases in HEAs. Numerous studies have been conducted by Murty and S. Ranganathan [36] to determine the effects of various milling parameters on the microstructure and properties of HEAs. These variables include the kind of milling, ball-to-powder ratio, milling speed, and milling time. There is a chance of improving energy efficiency for the mass production of HEAs by altering the milling parameters, such as the milling time, speed and process regulating agents, milling type (dry and wet milling), and ball-to-powder ratio. Moreover, the development of high-density dislocations, grain boundaries, and the micro-segregation of solutes at these defects may lead to an extended solid solution [37]. Varalakshmi et al. [38] employed high-energy mechanical milling to produce the first AlCrCuFeTiZn HEAs with a BCC structure and crystallite size of roughly 10 nm. They stated that the alloys remained stable throughout a 60 min annealing process at 800 °C. The FeCoNiAlCr high entropy alloy powder was also created by Gómez-Esparza et al. [39] using MA. After ten hours of milling, the powder showed a mixture of solid solution phases of FCC and BCC. A HEA-$FeCoNiB_{0.5}Si_{0.5}$ alloy was successfully created in a relatively recent work by mechanical alloying at 150 h with a single solid solution structure, even though the thermodynamic requirements for creating such a phase were not met [8]. The authors stated that two solid solutions were generated after 25 h of milling: a major BCC supersaturated solid solution and a minor FCC supersaturated solid solution.

Table 1. Various fabrication methods of certain HEAs and their resulting microstructures, the phase (s) obtained, and the corresponding mechanical properties.

HEA-Alloy	Observed Phase(s) Through Different Processing Route(s)			Strengthening Mechanism in Respective Processing Route(s)			Effects on Mechanical Properties		
	Melting and Casting	MA + SPS	AM	Melting and Casting	MA + SPS	AM	Melting and Casting	MA + SPS	AM
CoCrFeNiMn	FCC [18]	FCC [19]	FCC + BCC [20]		Solid solution strengthening	Grain boundary strengthening		Compressive strength of 1987 MPa Hardness of 646 HV	Tensile strength of 601 MPa
CoCrFeNiAl0.3	FCC [21]	FCC + BCC [22]	FCC [23]	Grain boundary strengthening	Solid solution strengthening	Dislocation hardening	UTS of 528 MPa YTS of 275 MPa	Compressive strength of 1907 MPa Hardness of 625 HV	YS of 730 MPaUTS of 896 MPa
AlCoCrCuFeNi	FCC + BCC [24]	FCC + BCC [25]	BCC [26]	Solid solution strengthening	Grain boundary strengthening, solid solution strengthening		Hardness of 515.5 HV (5.056 GPa) Compressive strength of 1.82 GPa	Hardness of 8.13 GPa Elastic modulus of 172 GPa	
Ni1.5Co1.5CrFeTi0.5	FCC [27]	FCC [28]		Solid solution hardening	Grain boundary strengthening		YS of 896 MPa Compressive strength of 1502 MPa Hardness of 515 HV	Hardness of 442 HV0.3 Tensile strength of 1384 MPa Elastic modulus of 216 GPa	
FeCoCrNiMnTi0.1C0.1			FCC [29]						
FeCrNiCoMn	FCC [30]			Grain boundary strengthening			Increase in yield strength from 200 to 350 MPa		

According to recent investigations [40,41], HEAs made of ferromagnetic materials (Fe, Co, and Ni) frequently show good soft magnetic properties, as well as exceptional mechanical qualities. It has been found through experiments that adding specific alloying elements to HEAs significantly affects the microstructure, structure, and characteristics of the resulting HEAs [42–44]. According to Zuo et al. [42], the saturation magnetization (Ms) of the FeCoNi alloy decreased more sharply when Si was added (from 151.3 to 80.5 emu/g) than when Al element was added (from 151.3 to 101.8 emu/g) [6]. In contrast to the Al element, the addition of Si to FeCoNi considerably increased the electrical resistivity [43]. Additionally, Zuo et al. observed that the value of Ms increased from 18.14 to 147.86 emu/g, 80.43 emu/g, and 80.29 emu/g, respectively, with the addition of Al, Ga, and Sn to the FeCoNiMn alloy [44]. Furthermore, recent magnetization experiments upon Al addition to FeCoNiCr HEA have shown a progressive transition from a paramagnetic to a ferromagnetic magnetic state at ambient temperature [45]. In conclusion, there are significant correlations between the alloying elements, the alloy's final crystal structure, and the magnetic characteristics of HEAs. Moreover, the influence of an additional component on phase formation and alloy characteristics, however, depends on several variables, including atomic radius, crystal structure, and enthalpy of mixing with other components.

The current work aims to manufacture FeCoNiMnTi HEA and investigate the effect of milling duration in the mechanical alloying process. X-ray diffraction (XRD), scanning electron microscopy (SEM) coupled with energy-dispersive X-ray spectroscopy (EDS), and a vibrating sample magnetometer (VSM) were used to examine the phase development, microstructure, and magnetic characteristics of the mechanically alloyed FeCoNiMnTi HEA for 100 h.

2. Materials and Methods

A high-energy planetary ball mill (Fritsch Pulverisette P7, FRITSH GmbH, Idar-Oberstein, Germany) was used to mechanically mill elemental powders of Fe, Co, Ni, Mn, and Ti (purity = 99.7%; particle size $\leq$ 30 μm; from Alpha Aesar) in an argon atmosphere to achieve the desired composition $Fe_{30}Co_{20}Ni_{20}Mn_{20}Ti_{10}$ (at %). Experiments involving ball milling were conducted in a harder steel container. The milling speed was set at 600 rpm, and the ball-to-powder weight ratio was kept at 0.47. Powder agglomeration and adhering to the container walls and balls were avoided by using a milling sequence that involved 10 min of milling followed by 5 min of idle time.

Using CuKα radiation, XRD measurements were performed on a Siemens D500 powder diffractometer (Siemens, Berlin, Germany) in ($\theta-2\theta$) geometry to characterize the structural and microstructural alterations of the milled powders. A full pattern XRD Rietveld fitting process revealed microstructural characteristics [46,47]. Using scanning electron microscopy (SEM, DSM960A ZEISS, Carl Zeiss GmbH, Oberkochen, Germany) in secondary electron mode at a voltage of 15 kV, the morphology of the alloy powders was examined. A Vega Tescan energy dispersive X-ray spectrometry (EDS) (Siemens, Berlin, Germany) was installed in the SEM. The software Image J (version 1.51j8, National Institutes of Health, Bethesda, MD, USA) was used to calculate the powder's particle size.

A superconducting quantum interference device from Quantum Design (Caledonia, MI, USA) SQUID MPMS-XL was used to measure the saturation magnetization (Ms), remanence (Mr), coercive field (Hc), and squareness ratio (Mr/Ms) of the as-milled and heat-treated powders at 300 K with a maximum applied field of 50 kOe.

3. Results and Discussion

3.1. SEM Analysis

An overview of the SEM images of the alloyed $Fe_{30}Co_{20}Ni_{20}Mn_{20}Ti_{10}$ (at%) powder mixtures acquired before (Figure 1a) and after high-energy mechanical milling for 4, 10, 20, 50, and 100 h of milling is provided in Figure 1b–f. Following a 4 h milling process, the powdered particles were cold-welded into larger ones with sizes ranging from 85 to 180 μm (Figure 1b). Nevertheless, because titanium is the softest and most ductile

metal, the titanium particles are severely deformed and can serve as a bonding agent to bind the hardest particles into agglomerates. Particles shapes might be polygonal or spherical. According to other reports [48,49], the final microstructure is the consequence of two deformation mechanisms: plastic deformation associated with cold-welding in ductile powders and fracture in hard powders, after milling periods of 10, 20, and 50 h (Figure 1c–e). The microstructure appears to be very fine after 100 h of milling, which could be the result of intense grain fracture as the grains get harder due to the progressive dissolution of metallic elements to form supersaturated solid solutions and the increase in work hardening (after severe plastic deformation and high level of crystallographic defects) (Figure 1f).

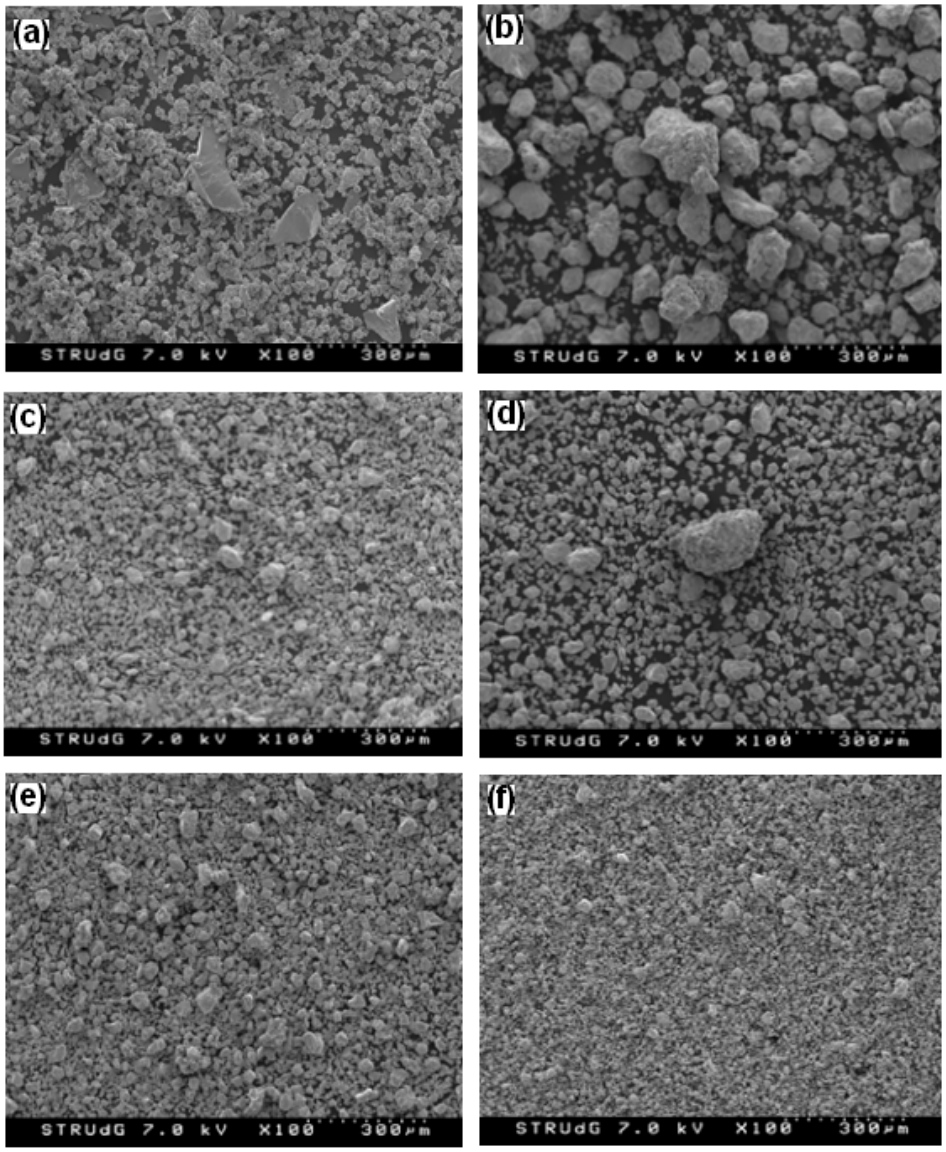

Figure 1. SEM images of the MA $Fe_{30}Co_{20}Ni_{20}Mn_{20}Ti_{10}$ powder mixtures as a function of milling times: (**a**) 0 h, (**b**) 4 h, (**c**) 10 h, (**d**) 20 h, (**e**) 50 h, and (**f**) 100 h.

3.2. XRD-Analysis

Figure 2 displays X-ray diffraction patterns of the $Fe_{30}Co_{20}Ni_{20}Mn_{20}Ti_{10}$ powder mixtures as a function of milling time. Figure 3 also displays the Rietveld refinements of the XRD patterns. There was always a goodness of fit (GOF) refinement parameter of 1.11. Controlling the alloying process was made possible by the subsequent diffraction patterns. The X-ray pattern of the unmilled powder is also given for comparison. Before

milling, the following peaks were measured: BCC-Fe (Im–3m; a_0 = 2.8667(1) Å), HCP-Co (P63/mmc; a_0 = 2.5071(1) Å and c_0 = 4. 0713(1) Å), FCC-Ni (Fm–3 m; a_0 = 3.5260(1) Å), BCC-Mn (I-43 m; a_0 = 8.9125(1) Å), and HCP-Ti (P63/mmc; a = 2.9064(1) Å and c = 4.6667(1) Å) (Figures 2 and 3).

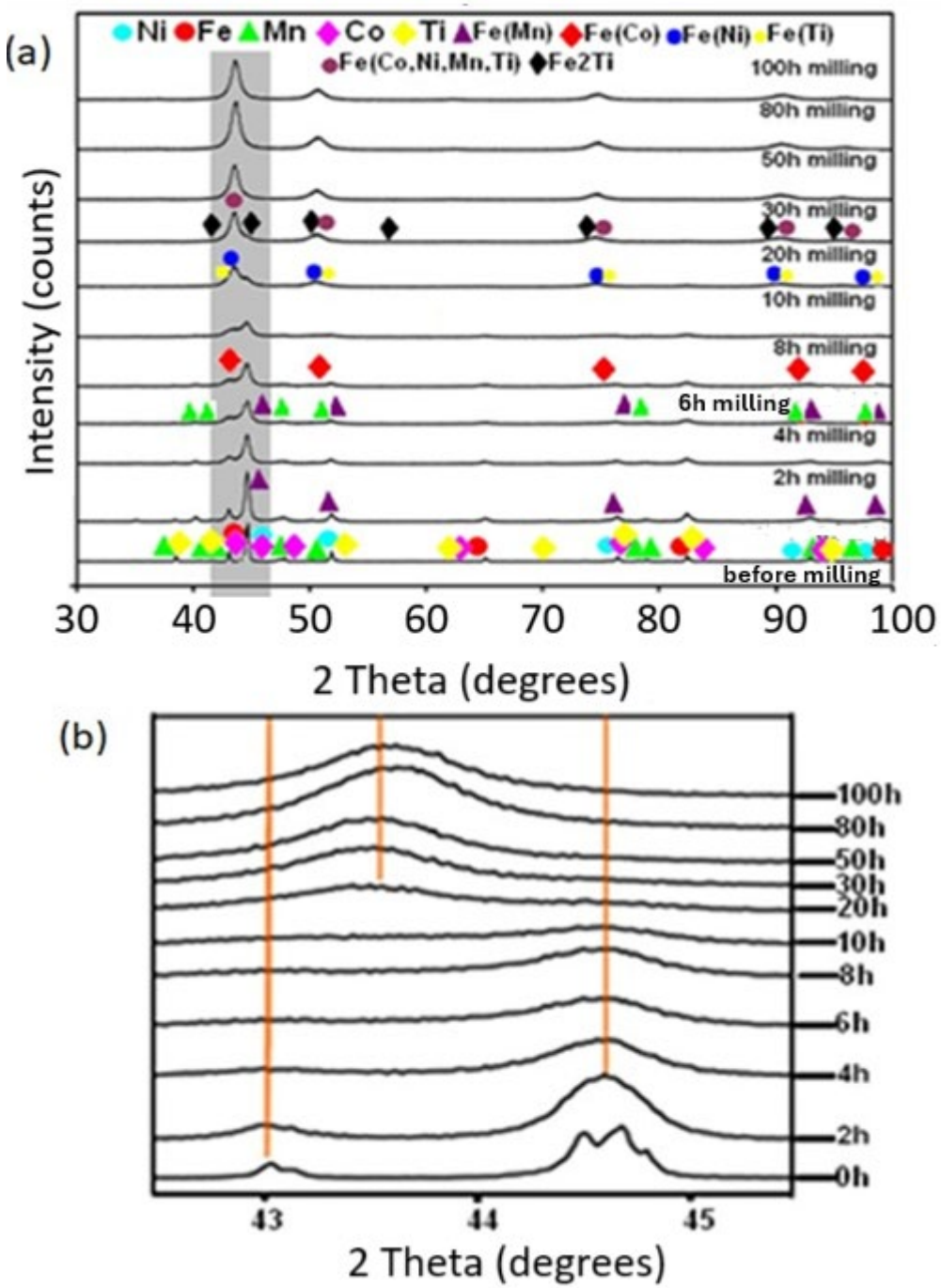

Figure 2. (**a**) XRD patterns (up) of the MA $Fe_{30}Co_{20}Ni_{20}Mn_{20}Ti_{10}$ powder mixtures as a function of milling times (in the bottom (**b**) a typical broadening and shifting of $(110)_{BCC}$ peaks).

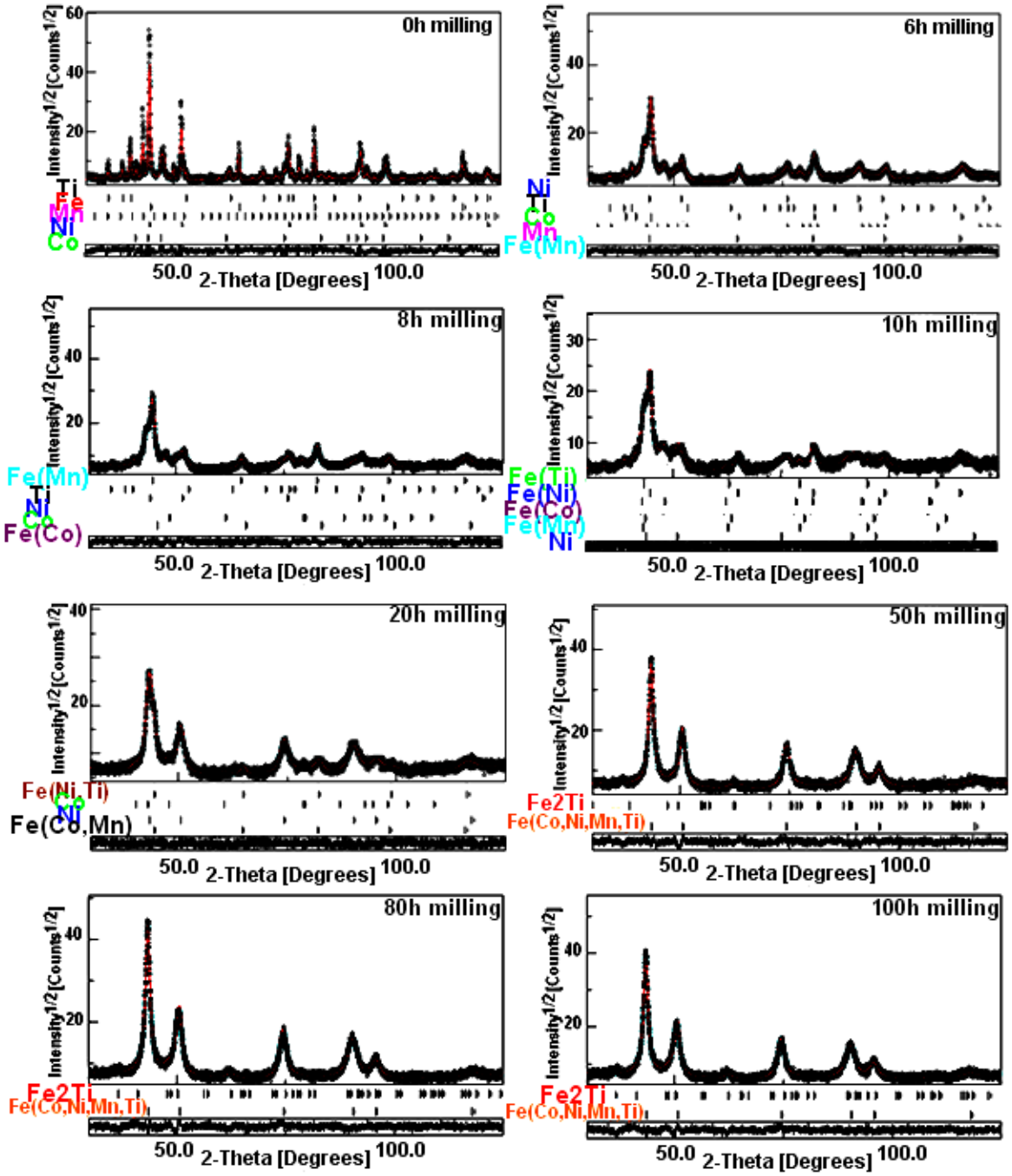

Figure 3. X-ray diffraction experimental patterns and the associated Rietveld theoretically adjusted MA $Fe_{30}Co_{20}Ni_{20}Mn_{20}Ti_{10}$ powders collected after selected milling times.

The metal peaks gradually vanished during milling, indicating that metals were dissolved in the Fe lattice by the MA (Figure 4). Furthermore, the profiles of the Fe diffraction peaks—particularly the (110) peak—become more asymmetrical and their low-angled shoulders broaden as the milling time increases. This could be explained by the appearance of broad, weakly intense peaks to the left of the Fe peaks. These shoulders can be ascribed to recently identified iron-based phases known as supersaturated solid solutions [16,50]. These phases exhibit characteristics with α-Fe in terms of structure, but they are distinguished by larger cell units, which means they have a slightly higher crystal parameter. Following 2 h of milling, the solid solution BCC-Fe(Mn)(Im–3m; a = 2.8679(1) Å; wt = 13%) initially appears. It continues for a maximum of 10 h, with a lattice parameter of a = 2.8674(1) Å and a proportion of 24%. Furthermore, after 8 h of milling, the development

of a BCC-Fe(Co) phase (Im–3m; a = 2.8666(1) Å, wt = 20%) takes place and can last for up to 10 h, with a lattice parameter of a = 2.8659(1) Å and a fraction of 28%. At this stage, with minority proportions of Co (a = 2.4411(1) Å, c = 4.0679(1) Å, and wt% = 8%) and Ni (a = 3.5685(1) Å, and wt = 10%), we were able to adequately fit the binary solid solutions BCC-Fe(Ni) (Im–3m; a = 2.8681(1) Å; wt = 15%) and BCC-Fe(Ti) (Im–3m; a = 2.9787(1) Å; wt = 14%). After 20 h of milling, BCC-Fe(Co,Mn) (a = 2.8746(1) Å) and BCC-Fe(Ni,Ti) (a = 2.8680(1) Å) were formed with proportions of 59% and 31%, respectively.

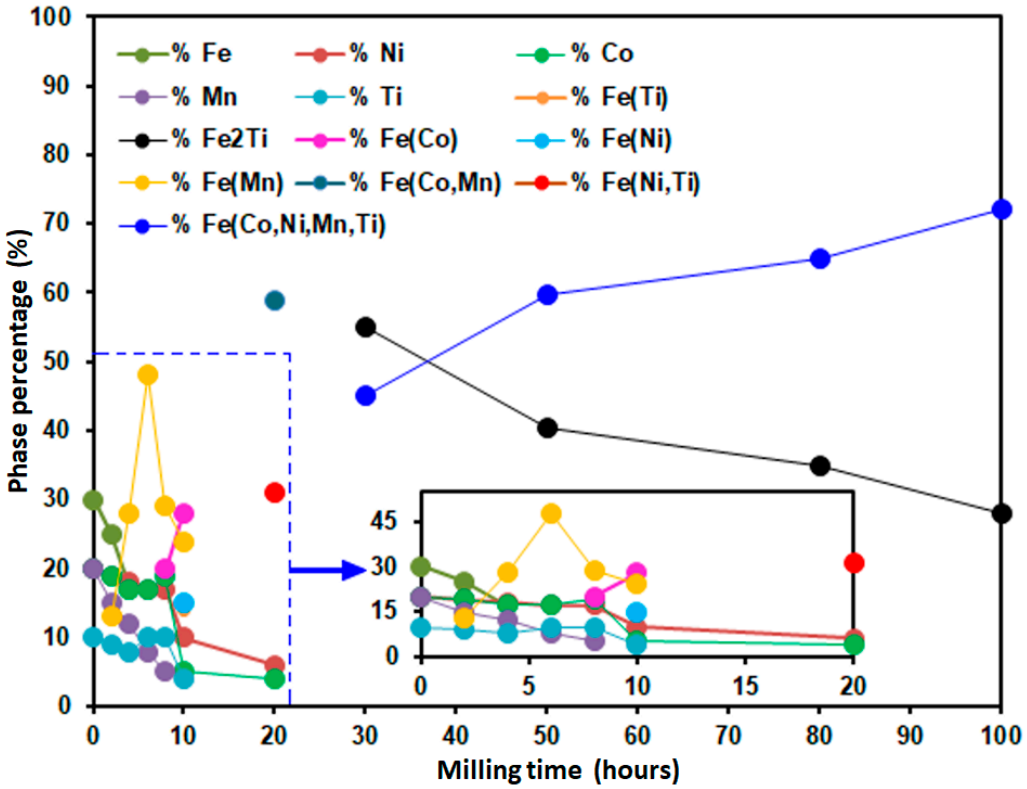

Figure 4. Variation in phase proportions as a function of milling time.

When we increase the milling time to 30 h, we see the formation of the BCC-Fe(Co,Ni,Mn,Ti) supersaturated solid solution, which has a phase proportion of about 45% and a lattice parameter of 3.6047(1) Å. Simultaneously, we refined the Fe_2Ti intermetallic with a 55% proportion adopting the C14 hexagonal (structure $MgZn_2$ type cell) with lattice parameters a = 4.7967(1) Å and c = 7.8330(1) Å). Even during longer milling times of 50, 80, and 100 h, one can observe that Fe_2Ti intermetallic remains, despite its proportion decreasing (from 55% for 30 h to 28% for 100 h). The Fe_2Ti intermetallic is now understood to fall into a specific composition range, designated as AB_2.

To achieve maximum space filling, the size and order of the A and B atoms are essential to the development of this stoichiometric phase. When $\frac{R_A}{R_B} = \sqrt{\frac{3}{2}} = 1.225$, the ratio of atomic radii is ideal for this to be achievable [51]. Simultaneously, a thorough refinement by Rietveld indicates that the proportion of the supersaturated solid solution Fe(Co,Ni,Mn,Ti) increases from 45% at 30 h of milling to 72% at 100 h. At this time difference (during an additional 70 h of milling), its crystalline parameter undergoes a relative variation of $\left(\frac{a_{100}-a_{30}}{a_{30}}\right) \times 100 = 0.5\%$ (a_{30} and a_{100} are lattice parameters calculated for 30 and 100 h milling, respectively). The reason for this lattice expansion might be attributed to the continuous diffusion of Co, Ni, Mn, and Ti into the BCC-Fe matrix, which caused the $(110)_{BCC}$ peak to be significantly displaced to the lower angle (Figure 2b). The increase in the density of lattice defects, or dislocations, with their distinctive strain fields on the nanocrystallite boundary, is another cause of this lattice expansion [52,53]. Additionally, the

lattice parameter variations may be associated with lattice disorder resulting from antisite defects (FeCo, FeNi, FeMn, FeTi, etc.). It has been stated that antisites and vacancies are the primary causes of the disorders in the B2 structure. The lattice parameter reduces when vacancies are the major defect; however, depending on the mismatch in the atomic volumes of the alloy components, the lattice parameter may increase if antisites are the predominant defect [54].

Since there were numerous defects during particle polishing with nanometric crystallites and a wide grain boundary domain, a significant amount of enthalpy may be maintained in nanocrystal alloys [55]. Therefore, the energy present in the deformation and grain boundaries of the crystalline lattice can facilitate the rapid formation of a solid solution. Moreover, the surface tension of nanometric crystals may cause the lattice to distort, enhancing the solubility. For elements with comparable concentrations, Chen et al. [55] found an inverse relationship between the melting points and alloying efficiencies. At lowering melting points, an element's diffusivity increases in the solid state [56]. The alloying rates of elements with virtually melting temperatures, including Fe (1811 K), Co (1768 K), Ni (1726 K), Mn (1792 K), and Ti (1941 K), are closely linked to the element's softness [55]. Moreover, the alloying rate of an element increases as the element concentration decreases [57]. Therefore, Ti → Mn → Co → Ni → Fe should be the order in which the elements in the FeCoNiMnTi HEA diffuse.

An additional observation in Figure 2 is the variations in the breadth of the diffraction peaks due to the lattice strain and crystallite size. The estimated mean crystallite size as a function of milling time is displayed in Figure 5. We can identify two distinct stages in the evolution of crystallite size: the sizes gradually diminish before 20 h of milling as the milling time increases, eventually settling within the 20–70 nm size population.

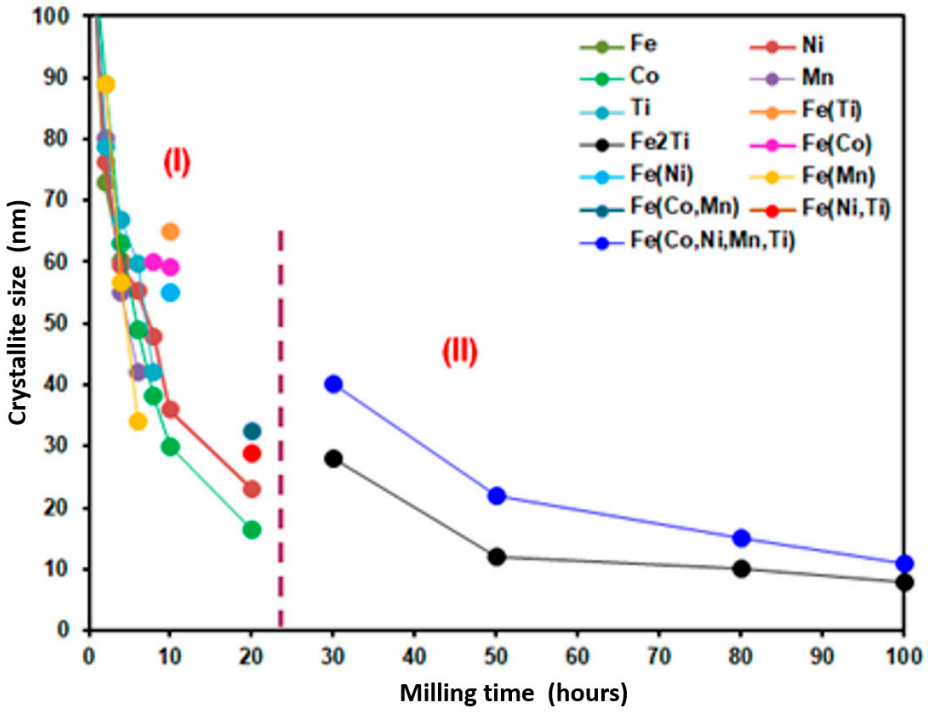

Figure 5. Variation of crystallite sizes and lattice strain values as a function of milling time of the different phases. Region I and region II before and after Fe_2Ti and Fe(Co,Ni,Mn,Ti) phases formation respectively.

The presence and disappearance of certain binary and ternary phases, each based on the degree of solubility of the metals after their dissolution into one another, characterize the production stage of the alloy represented by this population, as well as the other free elemental components that exist in every composition. Due to the influence of the

solid solution and the dynamic recrystallization of nanocrystals created by local heating during the mechanical alloying process, the BCC-FeCoNiMnAl phase is formed after 20 h (stage (II)) with a crystallite size of 40.5 nm greater than that of Fe(Co,Ni) (32 nm) and Fe(Ni,Ti) (29 nm) obtained after 20 h of milling [55,56]. After that, at the 100 h milling stage, it gradually decreases to a value of about 10 nm. Simultaneously, we note that the intermetallic hcp-Fe2Ti crystallites that appeared after 30 h of milling have a size estimated to be about 38 nm. After that, it decreases like that of BCC-Fe(Co,Ni,Mn,Ti) until its average value reaches approximately 8 nm. Conversely, the lattice strain levels for all elements rise progressively as a function of milling time during the first 20 h of milling (stage (I)) and reach values ranging from 0.7% (for Fe(Ti)) to 1.02% (for the Co element) (Figure 6). The values of the microdeformations progressively increase in the same manner when the MA process by-product is two-phase (after 20 h of milling), reaching a steady state after 80 h of milling with values of 1.15% and 0.95 for the phases BCC-Fe(Co,Ni,Mn,Ti) and Hcp-Fe_2Ti, respectively. As can be seen, all metallic systems generated by MA exhibit the characteristic pattern of increasing lattice strain level and decreasing crystallite size as the MA time increases [58].

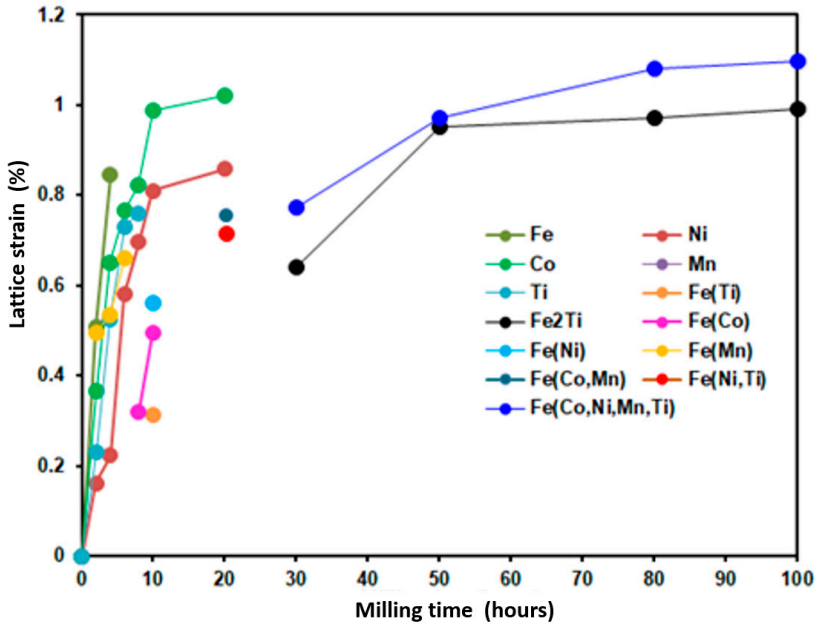

Figure 6. Variation of lattice strain values as a function of milling time.

The competition between the high degree of dynamic recovery in the deformed material and the rate of lattice strains produced by severe plastic deformation, following high-energy mechanical milling, is responsible for the formation of the nanocrystalline structure; in other words, this structure evolved from a dislocation cell structure. Lattice strain increases are often caused by significant dislocation densities and an increase in grain boundary proportion [57]. Dislocations are the main source of concern during the refining process. The early stages of deformation are characterized by the existence of dislocation cell blocks, which are divided by strong dislocation walls and contain dislocations grouped cellularly within the blocks. The density of massive dislocation walls rises, the internal dislocation structure becomes more random with less space for cellular structures, the size of the cell blocks gets closer to that of a cell, and the density of severe dislocation walls falls with increasing strain. The rise in residual strains in the material lattice may be attributed to the stress field associated with the dislocations' multiplication [59,60].

3.3. Magnetic-Analysis

A superposition hysteresis loop (M-H) for the MA $Fe_{30}Co_{20}Ni_{20}Mn_{20}Ti_{10}$ powder combinations is shown in Figure 7 as a function of the selected milling time. Similar hysteresis

loops were seen in all of the powdered samples, suggesting the presence of ferromagnetic behavior in these materials. In addition, each hysteresis cycle showed a sigmoidal form and a slight loss, which is consistent with the behavior observed in nanostructured samples containing small magnetic domains [16,61]. Moreover, soft magnetic materials must have exceptionally low hysteresis losses [16]. The reduced magnetization of the powder after 8 h of milling suggests the presence of the paramagnetic Ti atom, a substantial interatomic distance between magnetic atoms, and a high degree of disorder/defect structure.

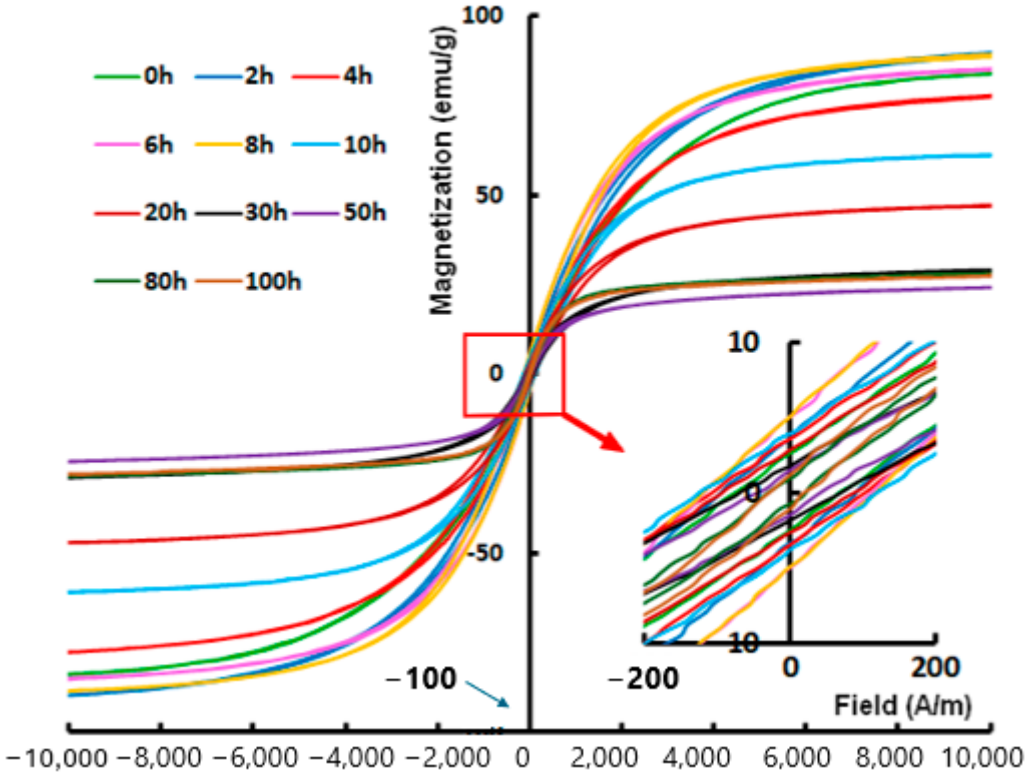

Figure 7. Typical hysteresis cycles (at 300 K) of the MA $Fe_{30}Co_{20}Ni_{20}Mn_{20}Ti_{10}$ powder mixtures as a function of milling times.

Coercivity

The intrinsic structure of the material has a substantial structural function, even though a large part of the intrinsic dependence of magnetic coercivity depends on magnetic anisotropy. Figure 8 illustrates how the behavior of the Hc changes as milling time increases. The majority of hard magnetic materials have Hc values up to 2800 Am^{-1} (35.18 Oe), whereas the majority of soft magnetic materials have Hc values of less than 1000 Am^{-1} (12.58 Oe) [61]. Based on the values of Hc that are obtained throughout the milling process (Hc~125 Am^{-1}) (1.57 Oe), one can first determine the degree of softness of the current materials. Furthermore, throughout the milling process, the two stages of change in the coercivity behavior—referred to as stages I and II—can be seen. The magnetic coercivity rises during the first 10 h (stage (I)) because extrinsic features, like micro-strain and crystalline size, which act as pinning sites, predominate. Nanocrystalline size reaches the critical value (about 15 nm) in 10 h, activating the Herzer model [62], which raises coercivity to 125 A/m^{-1}. According to this model, the structural correlation length (crystalline size) must be less than the exchange correlation length (Lex) for there to be magnetic softness in nanocrystalline alloys. Herzer revealed that the random anisotropy model explains the effective anisotropy energy even in nanocrystalline systems and predicted that the coercivity (Hc) changes as the sixth power of the crystallite size (D) throughout the range of D < Lex [63,64]. Furthermore, the Hc follows a 1/D-dependence law for

D < Lex. The coercivity determined by grain boundaries can be expressed as follows, as was previously described [65]:

$$Hc \approx 3\frac{\gamma_\omega}{M_s} \times \frac{1}{D} \quad (1)$$

where γ_ω is the wall energy and Ms is the saturation magnetization. The wall energy γ_ω can be estimated by the equation:

$$\gamma_\omega \approx \sqrt{\frac{k_B T_c K_1}{a}} \quad (2)$$

thus

$$H_c = 3 \times \sqrt{\frac{k_B T_c K_1}{aMs}} \times \frac{1}{D} \quad (3)$$

where k_B is the Boltzmann constant, K_1 is the magneto-crystalline anisotropy, T_c is the Curie temperature, and a is the lattice constant.

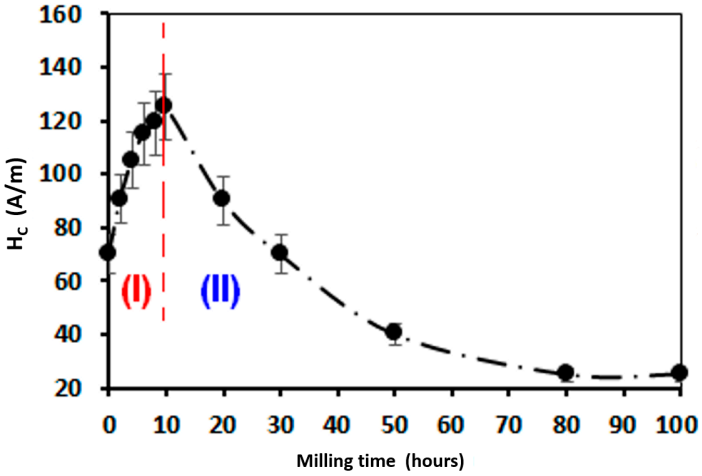

Figure 8. Variation of the coercivity (Hc) versus MA time, indicating I (increase) and II (decrease) stages.

The coercivity Hc starts to drastically decrease after 10 h of milling (it shows a polynomial reduction: Stage II) and reaches 25 Am^{-1} after 80 h. The decrease in Hc is ascribed to the crystalline size reduction effect, which overcomes the effect of microstrains in this milling time range since the crystalline size decreases with milling time [66]. As was previously mentioned, the reduction in magneto-crystalline anisotropy brought on by crystalline size refinement also makes it easier for the magnetization to rotate, which lowers Hc. The material exhibits a soft magnetic behavior (Hc around 25 Am^{-1}) and a very small crystallite size (about 10 nm at 100 h of milling) after 80 h of milling. It is crucial to emphasize that several factors, such as exchange interaction, magnetic anisotropy, demagnetization effects, surface conditions, and material structure, can affect the coercivity parameter [67,68]. The crystalline properties of alloys, microstrain, crystalline size, dislocation density, grain boundaries, residual stresses, free volumes, and microstructure in amorphous alloys all have an impact on the previously listed parameters [69,70]. Furthermore, a large number of nanocrystalline defects, primarily stacking faults, are produced within the crystal structure as a result of the notable deformation of the nanostructured powders. In the end, this results in a reduction in coercivity [71,72].

Conversely, the changes in saturation magnetization (Ms) with milling time provide additional insights into the mechanics of mechanical alloying. The characteristic that describes the atomic source of magnetism is called saturation magnetization. It is mostly dependent on the electrical structure of the atoms in the material and the chemical composition of the immediate environment. Exchange, crystal-field interaction, inter-atomic hopping,

and spin-orbit coupling are examples of quantum phenomena that are involved [73]. The change in saturation magnetization for the $Fe_{30}Co_{20}Ni_{20}Mn_{20}Ti_{10}$ powder mixture as a function of milling times is shown in Figure 9.

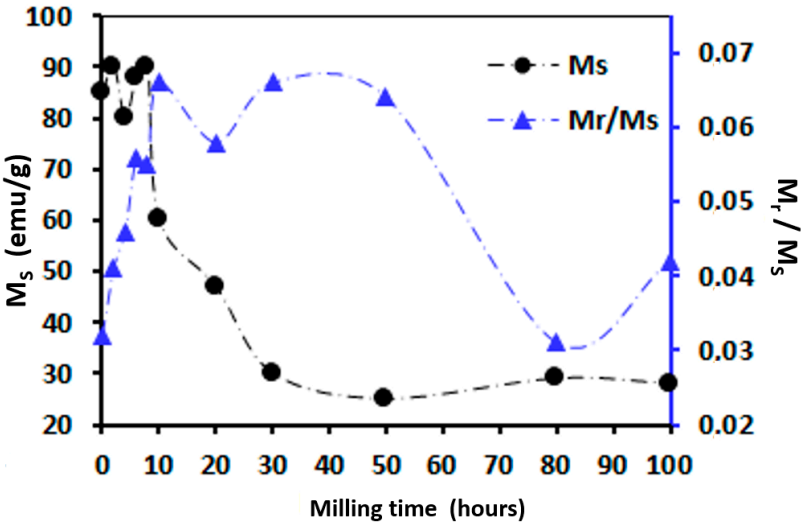

Figure 9. Variation of the saturation magnetization (Ms) and Mr/Ms ratio as a function of milling time.

To facilitate more productive conversations, this graph has been divided into two regions:

Region I: At the early stage, up to 8 h, the Ms takes its greatest values between 80 and 90 emu/g (varying in an oscillatory way within this interval of values). At this stage, changes in the fraction of the magnetic phases containing the magnetic components Fe, Co, Mn, Ni, and Ti that are present in the solid solution phases are often associated with variations in Ms. Because it raises the total magnetic moment per unit mass, the saturation magnetization increases with the proportion of magnetic phases [74,75]. As demonstrated by XRD examination, the Mn ($[Ar]4s^23d^5$ (M 5.9 B.M) atoms are dissolved into the Fe ($[Ar]4s^23d^6$ (4.89 B.M)) lattice at an early stage to form Fe(Mn) solid solution, which increases the Ms, whereas the dissolution of Co ($[Ar]4s^23d^7$ (M 3.7 μB)) or Ni ($[Ar]4s^23d^8$ (M 2.8 μB)) in the iron lattice can reduce the Ms.

Region II: M_S gradually decreases with milling time from 10 to 50 h. The reason for the rapid decrease is that the Fe_2Ti intermetallic and Fe(Co,Mn,Ni,Ti) solid solutions are formed when Ni and Ti dissolve in the Fe lattice. Ti metal is found to be weakly magnetic (in comparison to other ferromagnetic materials), and as a result, the density of the magnetic atom interactions is decreased when it dissolves in the lattices and reduces the proportion of magnetic atoms. Due to the reduction in d-band charge transfer and d-d hybridization, which reduces the number of polarization d states, there is less exchange interaction between Ti atoms and Fe–Ti, which suppresses the Fe metal moment. Moreover, the ordering kinetics are slowed down and the magnetization is slightly decreased by the presence of the Ti element. The formation of high concentrations of defects and interfaces, which severely limit the mobility of domain walls, is another factor contributing to this decrease in Ms values [50,76].

Region III: After the mixture has stabilized with the production of a two-phase system of BCC-Fe(Co,Mn,Ni,Ti) and the HCP-Fe_2Ti intermetallic, Ms takes on more or less steady values, ranging from 25 emu/g in 50 h to 28 emu/g in 100 h of milling. This occurs from 50 up to 100 h of milling times. A decrease in the interatomic distance between magnetic atoms and the partial crystallization intermetallic phase may be the cause of the small rise of 3 emu/g.

An essential magnetic measurement for determining the magnetic energy is the remanence-to-saturation ratio (Mr/Ms). The majority of the changes in the Mr/Ms ratio are caused by processing conditions, and the microstructural change that the metallic

system experiences during mechanical alloying explains these variations. For all samples processed by MA, the (Mr/Ms) ratio typically has a range of values between 0.032 and 0.066 (Figure 9). Nevertheless, it has been observed that in single-domain crystals with uniaxial anisotropy, the reduced remanence is of the order of 0.5 [77]. This implies that the magnetic crystals retain a multi-domain structure even if the crystallite sizes are in the nanometer range. In addition, the Mr/Ms ratio increases from 0.032 before milling, to 0.066 after 10 h, then decreases to 0.042 following 100 h of milling. Such behavior is consistent with previously reported alterations in coercivity (Figure 8). The decrease in domain wall energy and/or the phase change from coexisting multiphases before 10 h of milling to a major BCC and HCP phase following 10 h are likely the causes of this decrease. By reducing the stress-induced anisotropy, the prolonged mechanical milling of the powder mixture enhances the alloy's magnetic softening process. On the other hand, the $Fe_{30}Co_{20}Ni_{20}Mn_{20}Ti_{10}$ alloy powder exhibits soft magnetic properties, with a remanence ratio of 0.042, a saturated magnetization Ms of 28 emu/g, and a coercivity of 25 Am^{-1}.

4. Conclusions

The impact of milling time on the microstructural and magnetic properties of $Fe_{30}Co_{20}Ni_{20}Mn_{20}Ti_{10}$ (at%) produced via the mechanical alloying method was investigated in the current study using X-ray diffraction, scanning electron microscopy, and vibrating sample magnetometer techniques. The microstructural parameters were estimated using Rietveld refinement. Analysis indicates that a milling period of up to 30 h is necessary for phase change. At higher periods, the system preserves the two-phase structure: BCC-FeCoNiMnTi supersaturated solid solution and HCP-Fe_2Ti intermetallic. Furthermore, the estimated final average crystallite size (D) was around 10 nm, while the lattice strain (α) ranged from 0.95 to 1.15%. The magnetic characteristics were discovered to be connected to the microstructural changes. Following 100 h of milling, the powder was collected and its Ms value of 28 emu/g and Hc value of 25 Am^{-1} were found to be consistent with outstanding soft magnetics. This is mostly because of the formation of the BCC-Fe-based solid solution, the Fe_2Ti intermetallic, and the crystalline size refinement. Moreover, the low value of Ms has been linked to the occurrence of high densities of defects and interfaces, as well as the existence of paramagnetic Ti atoms in solid solution.

Author Contributions: Conceptualization, M.K. and J.-J.S.; methodology, M.K. and J.-J.S.; software, C.B.A., N.K. and M.A.; validation, M.C., M.K. and J.-J.S.; formal analysis, M.A., A.A. and M.C.; investigation, data curation, C.B.A., M.C. and A.A. writing—original draft preparation, C.B.A., N.K., and M.K.; writing—review and editing, M.K. and J.-J.S.; visualization, M.K. and M.C.; supervision, M.C. All authors have read and agreed to the published version of the manuscript.

Funding: This research received no external funding.

Data Availability Statement: The raw data supporting the conclusions of this article will be made available by the authors on request.

Conflicts of Interest: The authors declare no conflicts of interest.

References

1. Raja, R.K.; Sinha, S.K. Synthesis and phase investigation of equiatomic AlCrFeMnNi alloys dispersed with partially stabilized zirconia for nuclear applications. *Mater. Sci. Forum* **2020**, *978*, 145–151. [CrossRef]
2. Li, W.; Xie, D.; Li, D.; Zhang, Y.; Gao, Y.; Liaw, P.K. Mechanical behavior of high-entropy alloys. *Prog. Mater. Sci.* **2021**, *118*, 100777. [CrossRef]
3. Li, Z.; Zhao, S.; Ritchie, R.O.; Meyers, M.A. Mechanical properties of high-entropy alloys with emphasis on face-centered cubic alloys. *Prog. Mater. Sci.* **2019**, *102*, 296–345. [CrossRef]
4. Wu, Y.; Zhang, F.; Yuan, X.; Huang, H.; Wen, X.; Wang, Y.; Lu, Z. Short-range ordering and its effects on mechanical properties of high-entropy alloys. *J. Mater. Sci. Technol.* **2021**, *62*, 214–220. [CrossRef]
5. Yeh, J.W. *Overview of High-Entropy Alloys, High-Entropy Alloys, Fundamentals and Applications*; Gao, M.C., Yeh, J.W., Liaw, P.K., Zhang, Y., Eds.; Springer: Cham, Switzerland, 2016.

6. Miracle, B.D.; Senkov, O.N. A critical review of high entropy alloys and related concepts. *Acta Mater.* **2017**, *122*, 448–511. [CrossRef]
7. Yeh, J.W.; Chen, S.K.; Lin, S.J.; Gan, J.Y.; Chin, T.S.; Shun, T.T.; Tsau, C.H.; Chang, S.Y. Nanostructured high-entropy alloys with multiple principal elements: Novel alloy design concepts and outcomes. *Adv. Eng. Mater.* **2004**, *6*, 299–303. [CrossRef]
8. Cantor, B.; Chang, I.T.H.; Knight, P.; Vincent, A.J.B. Microstructural development in equiatomic multicomponent alloys. *Mater. Sci. Eng. A* **2004**, *375–377*, 213–218. [CrossRef]
9. Zaara, K.; Chemingui, M.; Gallet, S.L.; Gaillard, Y.; Escoda, L.; Saurina, J.; Suñol, J.J.; Bernard, F.; Khitouni, M.; Optasanu, V. High-Entropy FeCoNiB0.5Si0.5 Alloy Synthesized by Mechanical Alloying and Spark Plasma Sintering. *Crystals* **2020**, *10*, 929. [CrossRef]
10. Guo, S.; Liu, C. Phase stability in high entropy alloys: Formation of solid-solution phase or amorphous phase. *Prog. Nat. Sci.* **2011**, *21*, 433–446. [CrossRef]
11. Konakoglou, K.; Mathieu, C.; Georgatis, E.; Georgarakis, K.; Karantzalis, A.E. (FeMnNi)84(AlTi)16 High-Entropy Alloy: Correlation of Microstructure, Strengthening Mechanisms and Hardness at Various Conditions (As-Cast, Solution Treated, Aged). *Metallogr. Microstruct. Anal.* **2022**, *11*, 309–326. [CrossRef]
12. Ma, L.; Gao, Z.; Hu, S.; Zeng, Z.; Xu, J.; Wang, J. Effect of cooling rate on microstructure and mechanical properties of Al0.3CoCrFeNi high-entropy alloy. *Mater. Res. Express* **2019**, *6*, 056540.
13. Rogal, Ł. Semi-solid processing of the CoCrCuFeNi high entropy alloy. *Mater. Des.* **2017**, *119*, 406–416. [CrossRef]
14. Daly, R.; Khitouni, M.; Kolsi, A.W.; Njah, N. The studies of crystallite size and microstrains in aluminum powder prepared by mechanical milling. *Phys. Status Solidi (C)* **2006**, *3*, 3325–3331. [CrossRef]
15. Avila-Rubio, M.A.; Baldenebro-Lopez, J.A.; Soto-Rojo, R.; Ceballos-Mendivil, L.G.; Garza-Montes-de-Oca, N.F.; Baldenebro-Lopez, F.J. Effect of Mo and Ti on the microstructure and microhardness in AlCoFeNiMoTi high entropy alloys prepared by mechanical alloying and conventional sintering. *Adv. Powder Technol.* **2020**, *31*, 1693–1701. [CrossRef]
16. Ammar, C.B.; Khitouni, N.; Mbarek, W.B.; Alsulami, A.H.; Suñol, J.-J.; Khitouni, M.; Chemingui, M. Properties of High-Entropy Fe30Co20Ni20Mn20Al10 AlloyProduced by High-Energy Ball Milling. *Materials* **2024**, *17*, 234. [CrossRef]
17. Qiu, Z.; Yao, C.; Feng, K.; Li, Z.; Chu, P.K. Cryogenic deformation mechanism of CrMnFeCoNi high-entropy alloy fabricated by laser additive manufacturing process. *Int. J. Lightweight Mater. Manuf.* **2018**, *1*, 33–39. [CrossRef]
18. Pickering, E.J.; Muñoz-Moreno, R.; Stone, H.J.; Jones, N.G. Precipitation in the equiatomic high-entropy alloy CrMnFeCoNi. *Scr. Mater.* **2016**, *113*, 106–109. [CrossRef]
19. Ji, W.; Wang, W.; Wang, H.; Zhang, J.; Wang, Y.; Zhang, F.; Fu, Z. Alloying behavior and novel properties of CoCrFeNiMn high-entropy alloy fabricated by mechanical alloying and spark plasma sintering. *Intermetallics* **2015**, *56*, 24–27. [CrossRef]
20. Li, R.; Niu, P.; Yuan, T.; Cao, P.; Chen, C.; Zhou, K. Selective laser melting of an equiatomic CoCrFeMnNi high-entropy alloy: Processability, non-equilibrium microstructure and mechanical property. *J. Alloys Compd.* **2018**, *746*, 125–134. [CrossRef]
21. Lin, C.-M.; Tsai, H.-L. Evolution of microstructure, hardness, and corrosion properties of high-entropy Al0.5CoCrFeNi alloy. *Intermetallics* **2011**, *19*, 288–294. [CrossRef]
22. Ji, W.; Fu, Z.; Wang, W.; Wang, H.; Zhang, J.; Wang, Y.; Zhang, F. Mechanical alloying synthesis and spark plasma sintering consolidation of CoCrFeNiAl high-entropy alloy. *J. Alloys Compd.* **2014**, *589*, 61–66. [CrossRef]
23. Peyrouzet, F.; Hachet, D.; Soulas, R.; Navone, C.; Godet, S.; Gorsse, S. Selective Laser Melting of Al0.3CoCrFeNi High-Entropy Alloy: Printability, Microstructure, and Mechanical Properties. *JOM* **2019**, *71*, 3443–3451. [CrossRef]
24. Zhang, K.B.; Fu, Z.Y.; Zhang, J.Y.; Shi, J.; Wang, W.M.; Wang, H.; Wang, Y.C.; Zhang, Q.J. Annealing on the structure and properties evolution of the CoCrFeNiCuAl high-entropy alloy. *J. Alloys Compd.* **2010**, *502*, 295–299. [CrossRef]
25. Ganji, R.S.; Karthik, P.S.; Rao, K.B.S.; Rajulapati, K.V. Strengthening mechanisms in equiatomic ultrafine grained AlCoCrCuFeNi high-entropy alloy studied by micro-and nanoindentation methods. *Acta Mater.* **2017**, *125*, 58–68. [CrossRef]
26. Welk, B.A.; Williams, R.E.A.; Viswanathan, G.B.; Gibson, M.A.; Liaw, P.K.; Fraser, H.L. Nature of the interfaces between the constituent phases in the high entropy alloy CoCrCuFeNiAl. *Ultramicroscopy* **2013**, *134*, 193–199. [CrossRef] [PubMed]
27. Shun, T.-T.; Chang, L.-Y.; Shiu, M.-H. Microstructures and mechanical properties of multiprincipal component CoCrFeNiTix alloys. *Mater. Sci. Eng. A* **2012**, *556*, 170–174. [CrossRef]
28. Moravcik, I.; Cizek, J.; Zapletal, J.; Kovacova, Z.; Vesely, J.; Minarik, P.; Kitzmantel, M.; Neubauer, E.; Dlouhy, I. Microstructure and mechanical properties of Ni1,5Co1,5CrFeTi0,5 high entropy alloy fabricated by mechanical alloying and spark plasma sintering. *Mater. Des.* **2017**, *119*, 141–150. [CrossRef]
29. Liu, X.; Cheng, H.; Li, Z.; Wang, H.; Chang, F.; Wang, W.; Tang, Q.; Dai, P. Microstructure and mechanical properties of FeCoCrNiMnTi0.1C0.1 high-entropy alloy produced by mechanical alloying and vacuum hot-pressing sintering. *Vacuum* **2019**, *165*, 297–304. [CrossRef]
30. Otto, F.; Dlouhý, A.; Somsen, C.; Bei, H.; Eggeler, G.; George, E.P. The influences of temperature and microstructure on the tensile properties of a CoCrFeMnNi high-entropy alloy. *Acta Mater.* **2013**, *61*, 5743–5755. [CrossRef]
31. Huang, W.; Hou, J.; Wang, X.; Qiao, J.; Wu, Y. Excellent room-temperature tensile ductility in as-cast Ti37V15Nb22Hf23W3 refractory high entropy alloys. *Intermetallics* **2022**, *151*, 107735. [CrossRef]
32. Schuh, B.; Mendez-Martin, F.; Völker, B.; George, E.P.; Clemens, H.; Pippan, R.; Hohenwarter, A. Mechanical properties, microstructure and thermal stability of a nanocrystalline CoCrFeMnNi high-entropy alloy after severe plastic deformation. *Acta Mater.* **2015**, *96*, 258. [CrossRef]

33. Praveen, S.; Basu, J.; Kashyap, S.; Kottada, R.S. Exceptional resistance to grain growth in nanocrystalline CoCrFeNi high entropy alloy at high homologous temperatures. *J. Alloys Compd.* **2016**, *662*, 361. [CrossRef]
34. Zhang, Y.; Zuo, T.; Cheng, Y.; Liaw, P.K. High-entropy alloys with high saturation magnetization, electrical resistivity, and malleability. *Sci. Rep.* **2013**, *3*, 1. [CrossRef]
35. Chen, Z.; Chen, W.; Wu, B.; Cao, X.; Liu, L.; Fu, Z. Effects of Co and Ti on microstructure and mechanical behavior of Al0.75FeNiCrCo high entropy alloy prepared by mechanical alloying and spark plasma sintering. *Mater. Sci. Eng. A* **2015**, *648*, 217–224. [CrossRef]
36. Murty, B.S.; Ranganathan, S. Novel materials synthesis by mechanical alloying/milling. *Int. Mater. Rev.* **1998**, *43*, 101. [CrossRef]
37. Shashanka, R.; Chaira, D. Phase transformation and microstructure study of nano-structured austenitic and ferritic stainless-steel powders prepared by planetary milling. *Powder Technol.* **2014**, *259*, 125–136.
38. Varalakshmi, S.; Kamaraj, M.; Murty, B.S. Synthesis characterization of nanocrystalline AlFeTiCrZnCu high entropy solid solution by mechanical alloying. *J. Alloys Compd.* **2008**, *460*, 253–257. [CrossRef]
39. Gómez-Esparza, C.D.; Baldenebro-López, F.; González-Rodelas, L.; Baldenebro-López, J.; Martínez-Sánchez, R. Series of nanocrystalline NiCoAlFe (Cr, Cu, Mo, Ti) high entropy alloys produced by mechanical alloying. *Mater. Res.* **2016**, *19*, 39–44. [CrossRef]
40. Li, P.; Wang, A.; Liu, C.T. A ductile high entropy alloy with attractive magnetic properties. *J. Alloys Compd.* **2017**, *694*, 55–60. [CrossRef]
41. Zuo, T.; Gao, M.C.; Ouyang, L.; Yang, X.; Cheng, Y.; Feng, R.; Zhang, Y. Tailoring magnetic behavior of CoFeMnNiX (X = Al, Cr, Ga, and Sn) high entropy alloys by metal doping. *Acta Mater.* **2017**, *130*, 10–18. [CrossRef]
42. Mishra, R.K.; Shahi, R.R.J. Magn, Phase evolution and magnetic characteristics of TiFeNiCr and TiFeNiCrM (M = Mn, Co) high entropy alloys. *Magn. Mater.* **2017**, *442*, 218–223. [CrossRef]
43. Zuo, T.T.; Li, R.B.; Ren, X.J.; Zhang, Y.J. Magn, Effects of Al and Si addition on the structure and properties of CoFeNi equal atomic ratio alloy. *Magn. Mater.* **2014**, *371*, 60–68. [CrossRef]
44. Huang, S.; Li, W.; Li, X.; Schönecker, S.; Bergqvist, L.; Holmström, E.; Vitos, E.L. Mechanism of magnetic transition in FeCrCoNi-based high entropy alloys. *Mater. Des.* **2016**, *103*, 71–74. [CrossRef]
45. Lutterotti, L. Maud: A Rietveld Analysis program designed for the internet and experiment integration. *Acta Crystallografica Sect. A* **2000**, *56*, 54. [CrossRef]
46. Rietveld, H.M. A profile refinement method for nuclear and magnetic structures. *J. Appl. Crystallogr.* **1996**, *2*, 65–71. [CrossRef]
47. Suryanarayana, C.; Ivanov, E.; Boldyrev, V.V. The science and technology of mechanical alloying. *Mater. Sci. Eng. A.* **2001**, *304*, 151–158. [CrossRef]
48. Koch, C.C. Top-Down Synthesis of Nanostructured Materials: Mechanical and Thermal Processing Methods. *Rev. Adv. Mater. Sci.* **2003**, *5*, 91–99.
49. Girgis, K. *Physical Metallurgy*; Cahn, R.W., Hassen, P., Eds.; North-Holland Physics Publishing: Amsterdam, The Netherlands, 1983; p. 240.
50. Ibn Gharsallah, H.; Azabou, M.; Escoda, L.; Suñol, J.J.; López, I.; Llorca-Isern, N.; Khitouni, M. The magnetic and structural properties of nanostructured (Fe75Al25)100-xBx alloys prepared by mechanical alloying. *J. Alloys Compd.* **2017**, *729*, 776–786. [CrossRef]
51. Pfeiler, W. *Alloy Physics*; Wiley-VCH: Hoboken, NJ, USA, 2007; p. 861.
52. Zeng, Q.; Baker, I.; McCrearyand, V.; Yan, Z. Soft ferromagnetism in nanostructured mechanical alloying FeCo based powders. *J. Magn. Magn. Mater.* **2007**, *318*, 28–38. [CrossRef]
53. Mhadhbi, M.; Khitouni, M.; Escoda, L.; Suñol, J.J. X-ray studies of structure defects in nanostructured FeAl alloy. *Mater. Lett.* **2010**, *64*, 1802–1805. [CrossRef]
54. Zhang, K.; Fu, Z.; Zhang, J.; Wang, W.; Lee, S.; Niihara, K. Characterization of nanocrystalline CoCrFeNiTiAl high-entropy solid solution processed by mechanical alloying. *J. Alloys Compd.* **2010**, *495*, 33–38. [CrossRef]
55. Chen, Y.-L.; Hu, Y.-H.; Hsieh, C.-A.; Yeh, J.-W.; Chen, S.-K. Competition between elements during mechanical alloying in an octonary multi-principal-element alloy system. *J. Alloys Compd.* **2009**, *481*, 768–775. [CrossRef]
56. Porter, D.A.; Easterling, K.E. *Phase Transformations in Metals and Alloys*, 2nd ed.; Springer: Berlin, Germany, 1992.
57. Fu, Z.; Chen, W.; Chen, Z.; Wen, H.; Lavernia, E.J. Influence of Ti addition and sintering method on microstructure and mechanical behavior of a medium-entropy Al0.6CoNiFe alloy. *Mater. Sci. Eng. A.* **2014**, *619*, 137–145. [CrossRef]
58. Shokrollahi, H. The magnetic and structural properties of the most important alloys of iron produced by mechanical alloying Mater. *Mater. Des.* **2009**, *30*, 3374. [CrossRef]
59. Khitouni, M.; Kolsi, A.W.; Njah, N. The effect of boron additions on the disordering and crystallite refinement of Ni3Al powders during mechanical milling. *Ann. Chim. Sci. Mat.* **2003**, *28*, 17–29. [CrossRef]
60. Daly, R.; Sunol, J.J.; Khitouni, M. Structural thermal properties of the Fe-based alloys prepared by mechanical milling Korean. *J. Chem. Eng.* **2022**, *39*, 1614–1623.
61. Gutfleisch, O.; Willard, M.A.; Brück, E.; Chen, C.H.; Sankar, S.G.; Liu, J.P. Magnetic Materials and Devices for the 21st Century: Stronger, Lighter, and More Energy Efficient. *Adv. Mater.* **2011**, *23*, 821–842. [CrossRef]
62. Herzer, G. The Random Anisotropy Model. In *Properties and Applications of Nanocrystalline Alloys from Amorphous Precursors*; Idzikowski, B., Švec, P., Miglierini, M., Eds.; NATO Science Series; Springer: Dordrecht, The Netherlands, 2005; p. 184.
63. Herzer, G. Grain structure and magnetism of nanocrystalline ferromagnets. *IEEE Trans. Mag.* **1989**, *25*, 3327–3329. [CrossRef]

64. Herzer, G. Grain size dependence of coercivity and permeability in nanocrystalline ferromagnets. *IEEE Trans. Mag.* **1990**, *26*, 1397–1402. [CrossRef]
65. Yu, R.H.; Basu, S.; Ren, L.; Zhang, Y.; Parvizi-Majidi, A.; Unruh, K.M.; Xiao, J.Q. High temperature soft magnetic materials: FeCo alloys and composites. *IEEE Trans. Magn.* **2000**, *36*, 3388–3393. [CrossRef]
66. Hamzaoui, R.; Cherigui, M.; Guessasma, S.; Elkedimand, O.; Fenineche, N. Artificial neural network methodology: Application to predict magnetic properties of nanocrystalline alloys. *Mater Sci Eng.* **2009**, *163*, 17–21. [CrossRef]
67. Hedayatnasab, Z.; Abnisa, F.; Daud, W.M.A.W. Review on magnetic nanoparticless for magnetic nanofluid hyperthermia application. *Mater. Des.* **2017**, *123*, 174–196. [CrossRef]
68. Fidler, J.; Schrefl, T. Micromagnetic modelling-the current state of the art. *J. Phys. D Appl. Phys.* **2000**, *33*, R135. [CrossRef]
69. Fang, X.; Jin, G.; Cui, X.; Liu, J. Evolution characteristics of residual stress in metastable Ni-B alloy coatings identified by nanoindentation. *Surf. Coat. Technol.* **2016**, *305*, 208–214. [CrossRef]
70. Ortiz, A.; Tian, J.; Villegas, J.; Shaw, L.; Liaw, P. Interrogation of the microstructure and residual stress of a nickel-base alloy subjected to surface severe plastic deformation. *Acta Mater.* **2008**, *56*, 413–426. [CrossRef]
71. Triki, M.; Mechri, H.; Azzaz, H.; Azzaz, M. Characterization of nanostructured magnetic alloy based on Ni-Co-Mn produced by mechanical synthesis. *J. Magn. Magn. Mater.* **2022**, *541*, 168514. [CrossRef]
72. Xu, Y.; Sun, Y.; Dai, X.; Liao, B.; Zhou, S.; Chen, D. Microstructure and magnetic properties of amorphous/nanocrystalline $Ti_{50}Fe_{50}$ alloys prepared by mechanical alloying. *J. Mater. Res. Technol.* **2019**, *8*, 2486–2493. [CrossRef]
73. Miracle, D.B.; Sanders, W.S.; Senkov, O.N. The influence of efficient atomic packing on the constitution of metallic glasses. *Philos. Mag.* **2003**, *83*, 2409–2428.
74. Wang, J.; Zheng, Z.; Xu, J.; Wang, Y. Microstructure and magnetic properties of mechanically alloyed FeSiBAlNi (Nb) high entropy alloys. *J. Magn. Magn. Mater.* **2014**, *355*, 58–64. [CrossRef]
75. Tsai, M.H. Physical properties of high entropy alloys. *Entropy* **2013**, *15*, 5338. [CrossRef]
76. Burton, P.W. *A Handbook of Lattice Spacings and Structures of Metals and Alloys: International Series of Monographs on Metal Physics and Physical Metallurgy*, 1st ed.; Elsevier: Amsterdam, The Netherlands, 2013; Volume 4.
77. Zeng, Q.; Baker, I. Magnetic properties and thermal ordering of mechanically alloyed Fe–40 at% Al. *Intermetallics* **2006**, *14*, 396–405.